

# Supporting Information for “Upper Mantle Structure beneath the Contiguous US Resolved with Array Observations of SKS Multipathing and Slowness Vector Perturbations”

J. Ward <sup>1</sup>, M. Thorne <sup>2</sup>, A Nowacki <sup>1</sup>, S. Rost <sup>1</sup>

<sup>1</sup>School of Earth and Environment; University of Leeds

<sup>2</sup>Department of Geology and Geophysics; University of Utah

## Contents of this file

1. Text S1 to S7
2. Figures S1 to S19
3. Table S1

## Additional Supporting Information (Files uploaded separately)

1. Captions for Datasets S1

## Introduction

### Text S1. Break up sub array explanatory figure

We used an algorithm to automatically break station locations into smaller sub arrays. The process is illustrated in Figure S1. From the location of all the stations (a) applied DBSCAN (Ester et al., 1996) is applied to identify outlier stations which do not meet the density criteria (b). The outlier stations are then removed (c). To avoid many sub

arrays being created in one region, centroid stations are found which are not within a neighbourhood of another centroid station (d). From the centroid stations, take all the stations within the desired neighbourhood distance forming the sub arrays (e).

### **Text S2. Automated method explanatory figure**

Figure S2 shows the steps involved with the automated technique of Ward, Thorne, Nowacki, and Rost (2021).

### **Text S3. Explanatory figure of slowness vector RMS**

Figure S3 illustrates how the variance of slowness vector measurements is calculated.

### **Text S4. Model setup visualisation**

Figure S4 shows the model setup for the ray tracing.

### **Text S5. Effects of source-side structure on observations**

Our forward modelling shows very little slowness vector deviations for core-mantle boundary source side structures except for extreme mantle heterogeneities with velocity perturbations of  $\pm 10\% \delta V_S$  where slowness vector deviations of up to  $0.5 \text{ s}^\circ$  are observed (Figure S7). More realistic velocity anomalies show negligible anomalies ( $<0.2 \text{ s}^\circ$ ). Where heterogeneities exist on the source side, the seismically slow anomalies cause slowness vector deviations to converge and fast anomalies cause them to diverge (Figure S8). The opposite of what is seen on the receiver side. However as mentioned, the slowness vector deviations are negligible when realistic velocity perturbations of  $\pm 5\%$  are used.

Visual inspection of the observed source-side slowness vector bins show a distinct pattern (slowness vector magnitudes  $> 0.5 \text{ s}^\circ$ ) beneath the eastern Pacific only (Figure S6). The vectors vary smoothly with a slight convergence in the north of the area and then generally trending south-east to the south with large slowness vector deviation magnitudes

( $> 1.5s/\circ$ ). As this does not match an expected pattern of the seismically slow and fast anomalies we tested, we suggest this pattern is an artifact of complex wavefield interaction with the subducting slab near the surface on the source side or is caused by structure on the receiver side which, when projected onto the source side, causes this pattern.

#### **Text S6. Breakdown of number of observations by frequency band**

Table S1 shows the breakdown of the number of arrivals observed in different frequency bands.

#### **Text S7. Further modelling observations**

Figures ?? to ?? show the results of the forward modelling with different heterogeneities in the upper mantle on the receiver side. We find a larger seismic velocity anomaly and in these models also the seismic velocity gradient tends to increase the slowness vector perturbation. The  $-10\%\delta V_S$  example (Figure S10) is the exception here, but we expect this is because of the simplified modelling approach we used and the wavefield complexities caused by an extremely slow cylinder would not be captured by 3D ray tracing predicting the first arrival of an SKS wave.

A smaller anomaly (Figure S11) leads to a similar slowness vector perturbation but the deviations occur over a smaller area. In all models, the slowness vector deviation azimuths appear to be orthogonal to that of the boundary.

#### **Text S8. Summary plots of observations**

Figures S12 to S24 show the depth slices and frequency bands in Table S1 which were not shown in the main text.

#### **Data Set S1.**

The results are available as text file here: [10.6084/m9.figshare.21710603](https://doi.org/10.6084/m9.figshare.21710603).

## References

- Ester, M., Kriegel, H.-P., Sander, J., Xu, X., & others. (1996). A density-based algorithm for discovering clusters in large spatial databases with noise. In *Kdd* (Vol. 96, pp. 226–231).
- Ward, J., Thorne, M., Nowacki, A., & Rost, S. (2021, September). Automatic slowness vector measurements of seismic arrivals with uncertainty estimates using bootstrap sampling, array methods and unsupervised learning. *Geophysical Journal International*, 226(3), 1847–1857.

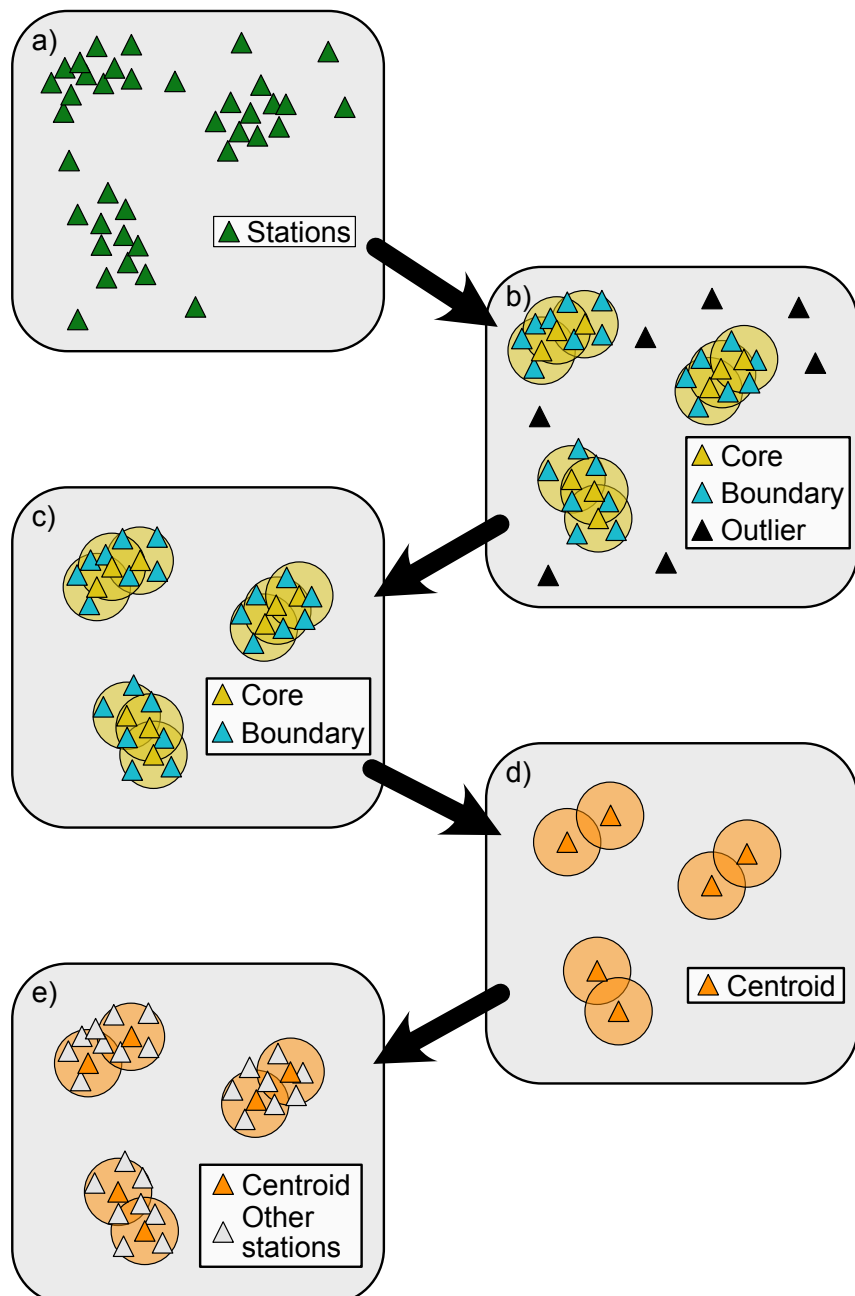


**Figure S1.** Cartoon describing the steps to automatically form a distribution of stations

(a) into sub-arrays (e).

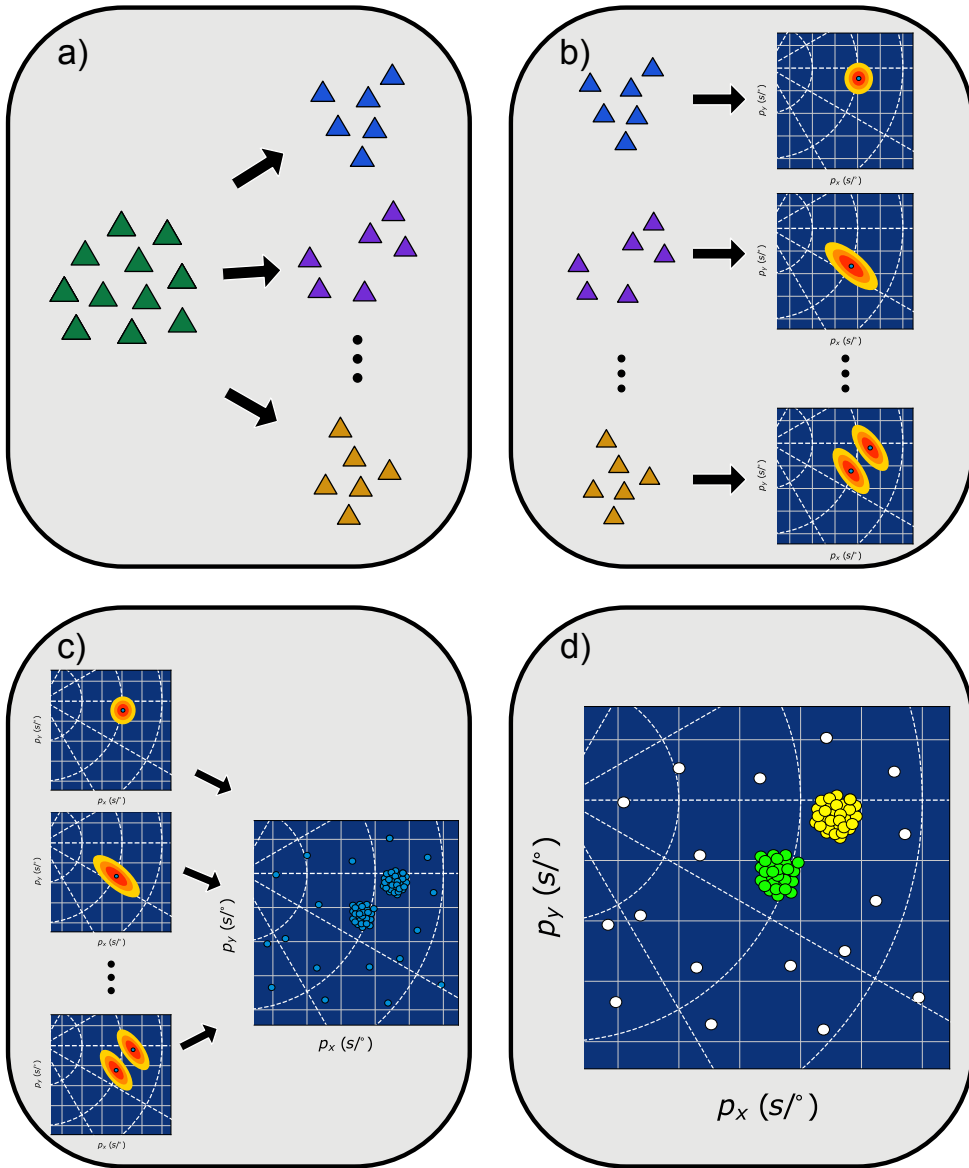


**Figure S2.** Cartoon describing the steps to automatically identify arrivals in slowness space and measuring their slowness vector properties. First bootstrap sample the traces recorded at an array 1000 times creating 1000 random sub arrays (a). Then, for each bootstrap sample, perform linear beamforming grid search and recover the top peaks (b). Once this is done, collect all the points from all 1000 samples (c). Finally, apply clustering algorithm DBSCAN (Ester et al., 1996) to identify regions dense enough to form clusters and, from their location, measure their slowness vector properties.

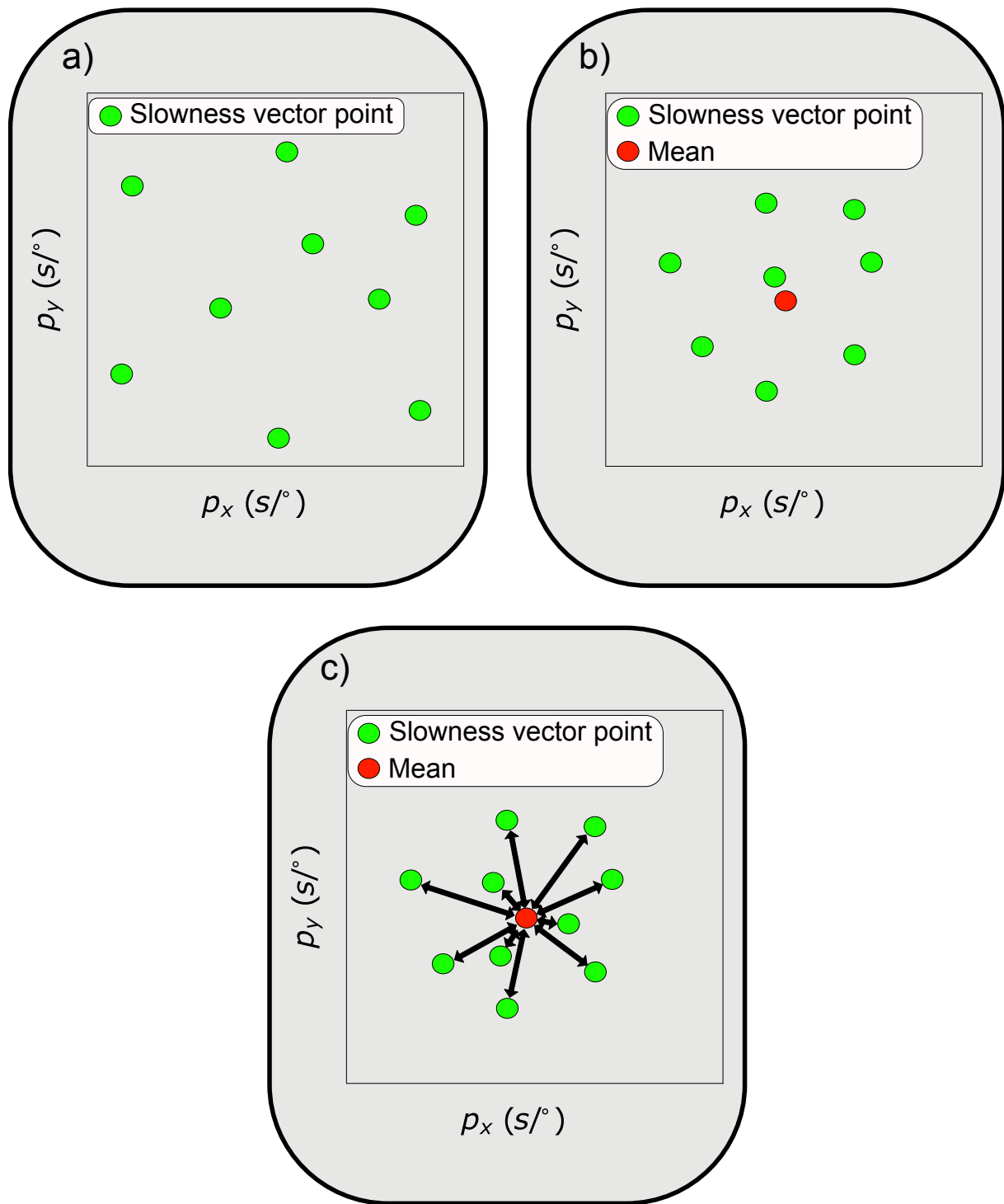


**Figure S3.** Cartoon of how from a cluster of slowness vector points in slowness space (a), the mean is measured (b) and the distances in slowness space are found (c). From these distances the RMS is calculated.

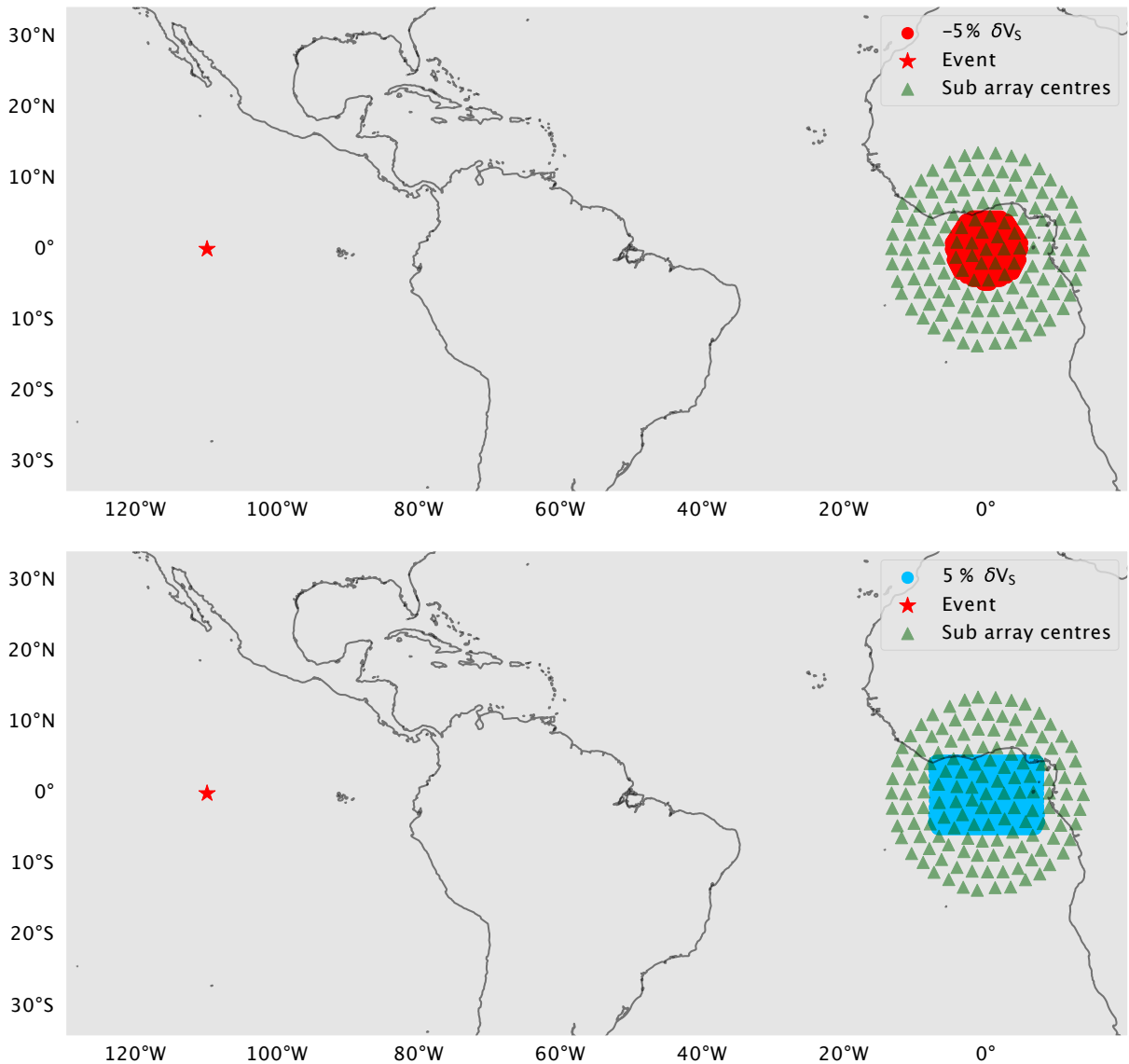


**Figure S4.** Model setups for the 3-D ray-tracing. through a slow cylinder with a diameter of 1000 km and a velocity perturbation of  $-5\% \delta V_S$  (top) and a fast cubiod with a length of 1500 km and a width of 1000 km, and a velocity perturbation of  $+5\% \delta V_S$  (bottom). Both of these anomalies are 300 km thick and extend from 100 km to 400 km depth. Also shown are the event location (red star) at  $-110^\circ$  longitude,  $0^\circ$  latitude and the mean station locations of the sub-arrays (green triangles).

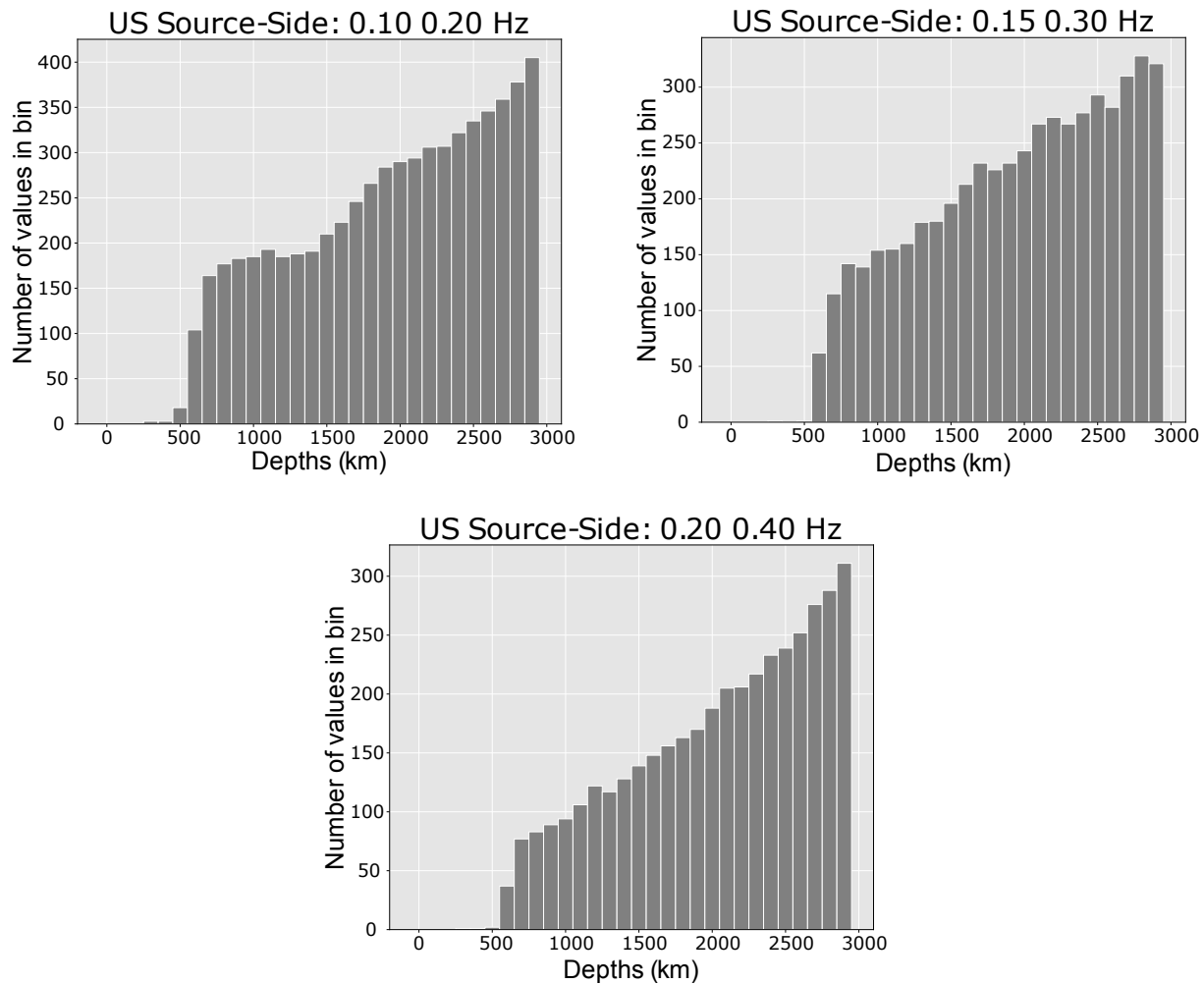


**Figure S5.** Histograms of the number of bins with a significantly low variance of slowness vector measurements (Section 2.3 in the main text) at each depth for bins on the source side. These have been separated by frequency band.

X - 10

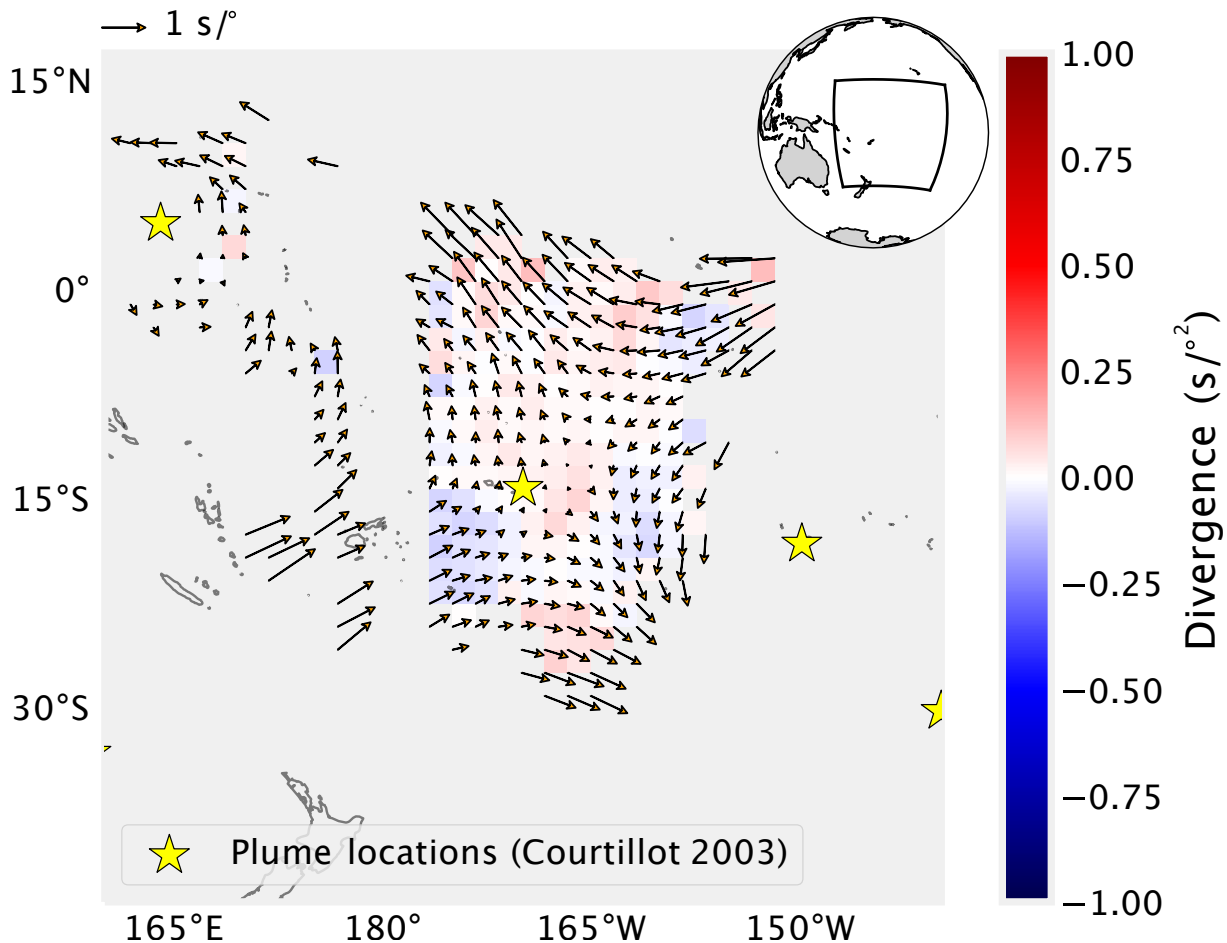


**Figure S6.** Map of slowness vector bins on the source-side beneath the southwest Pacific traveling to stations in North America. For reference a globe is added with the region marked (top right). The bins use pierce points at 2891 km depth and use data from the 0.10 – 0.20 Hz frequency band.

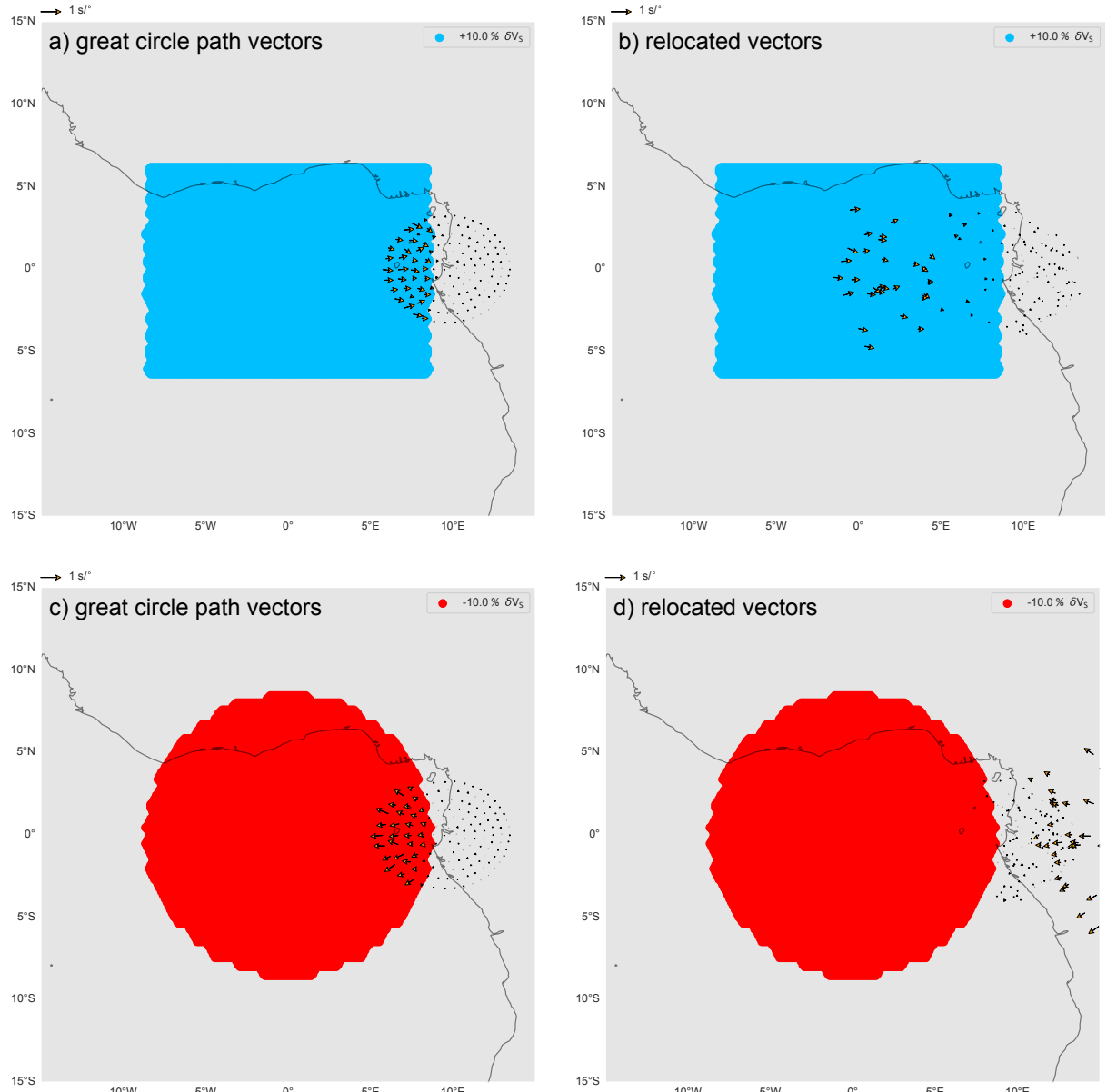


**Figure S7.** Modelling results for the effect of CMB heterogeneities on the source side with a cuboid of height 500 km, length of 1000 km and width 750 km and velocity anomaly of +10% (top) and a cylinder of height 500 km and radius 500 km with a velocity anomaly of -10% (bottom). The vectors have been plotted at their great circle path (left) and been relocated such that they arrive with the same backazimuth and horizontal slowness as the measured arrival (right).

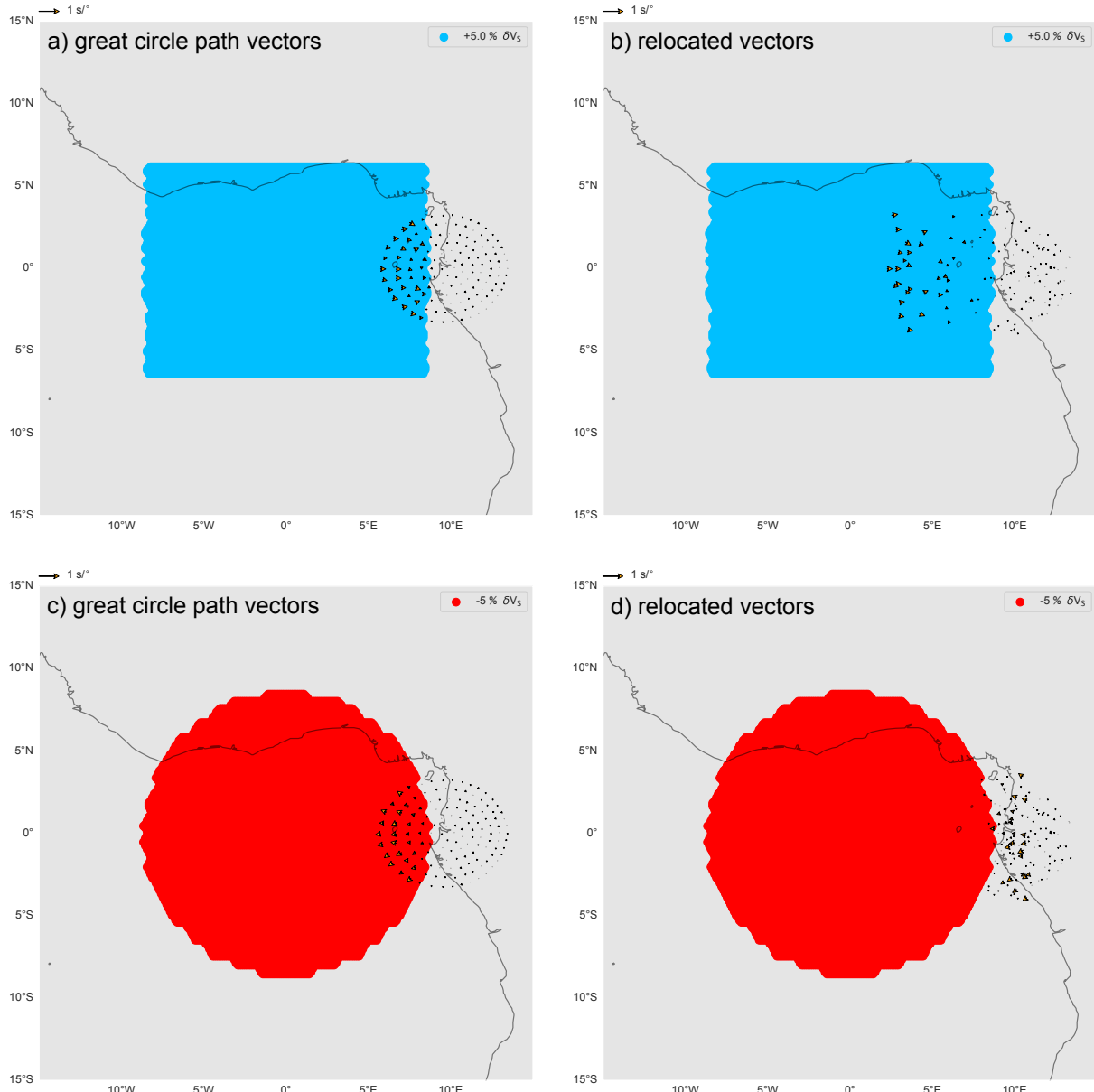


**Figure S8.** Modelling results for the effect of CMB heterogeneities on the source side with a cuboid of height 500 km, length of 1000 km and width 750 km and velocity anomaly of +5% (top) and a cylinder of height 500 km and radius 500 km with a velocity anomaly of -5% (bottom). The vectors have been plotted at their great circle path (left) and been relocated such that they arrive with the same backazimuth and horizontal slowness as the measured arrival (right).

**Table S1.** Number of observations labelled as having 1,2 or 3 arrivals in each frequency band.

Frequency Band (Hz)	Number of Arrivals Observed		
	1	2	3
0.10 – 0.20	2118	16	0
0.15 – 0.30	1851	108	4
0.20 – 0.40	1608	231	24

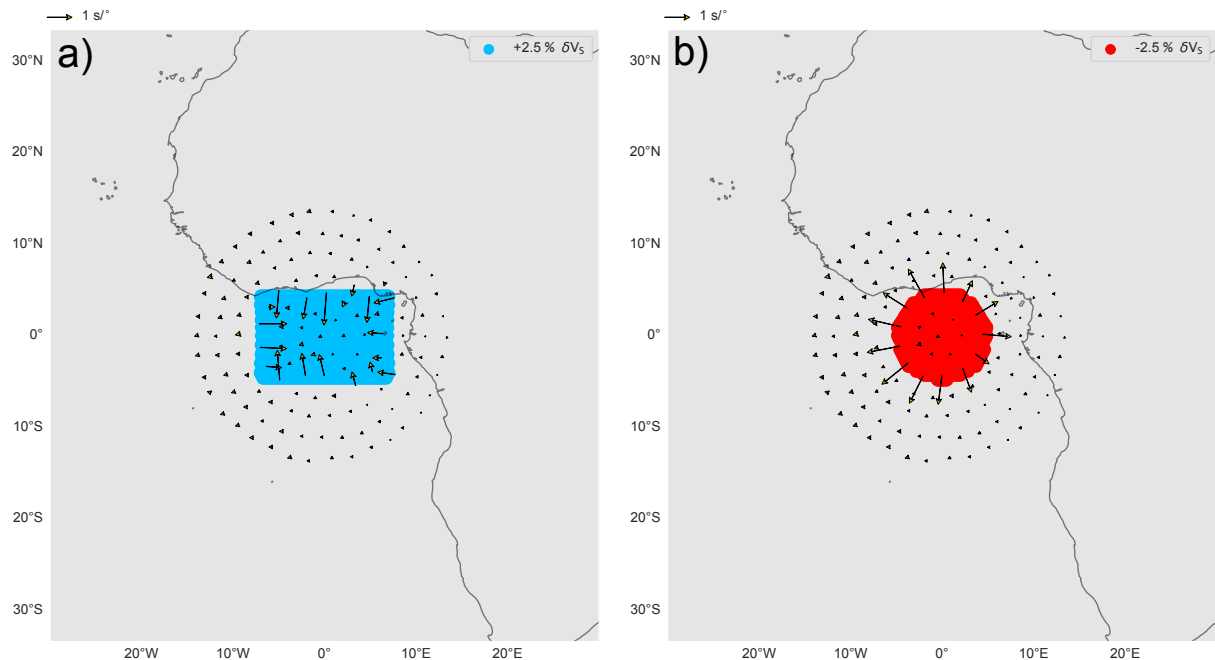


**Figure S9.** Modelling results for the effect of upper mantle heterogeneities with a cuboid with a depth extent of 300 km between 100 and 400 km depth, length of 1500 km and width 1000 km and velocity anomaly of +2.5% (a) and a cylinder with a depth extent of 300 km between 100 and 400 km depth, and radius 500 km with a velocity anomaly of -2.5% (b). The vectors have been plotted at their great circle path.

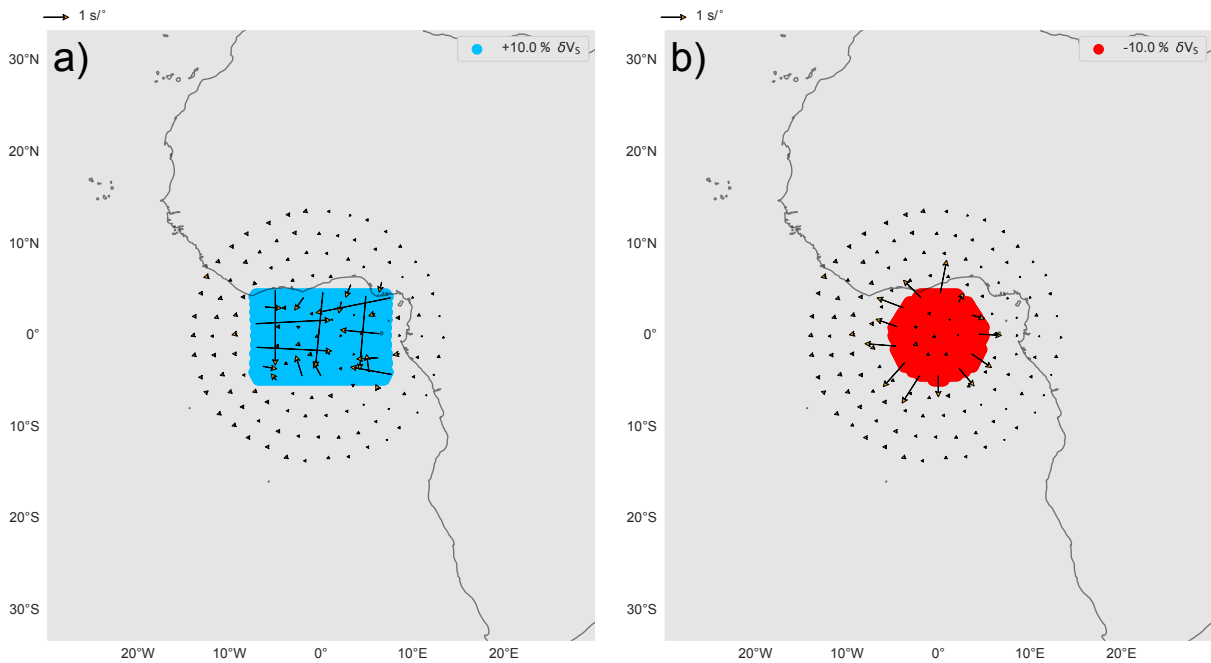


**Figure S10.** Modelling results for the effect of upper mantle heterogeneities with a cuboid with a depth extent of 300 km between 100 and 400 km depth, length of 1500 km and width 500 km and velocity anomaly of +10% (a) and a cylinder with a depth extent of 300 km between 100 and 400 km depth, and radius 500 km with a velocity anomaly of -10% (b).

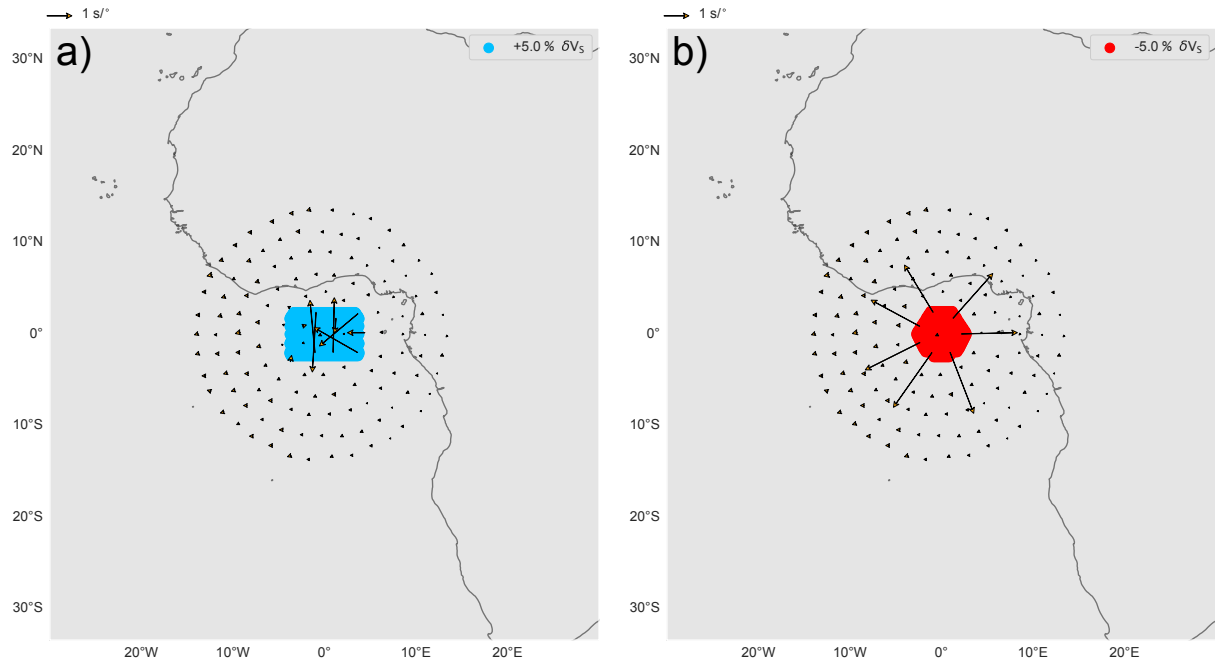


**Figure S11.** Modelling results for the effect of upper mantle heterogeneities with a cuboid with a depth extent of 300 km between 100 and 400 km depth, length of 500 km and width 250 km and velocity anomaly of +5% (a) and a cylinder with a depth extent of 300 km between 100 and 400 km depth, 300 km and radius 250 km with a velocity anomaly of -5% (b). The vectors have been plotted at their great circle path.

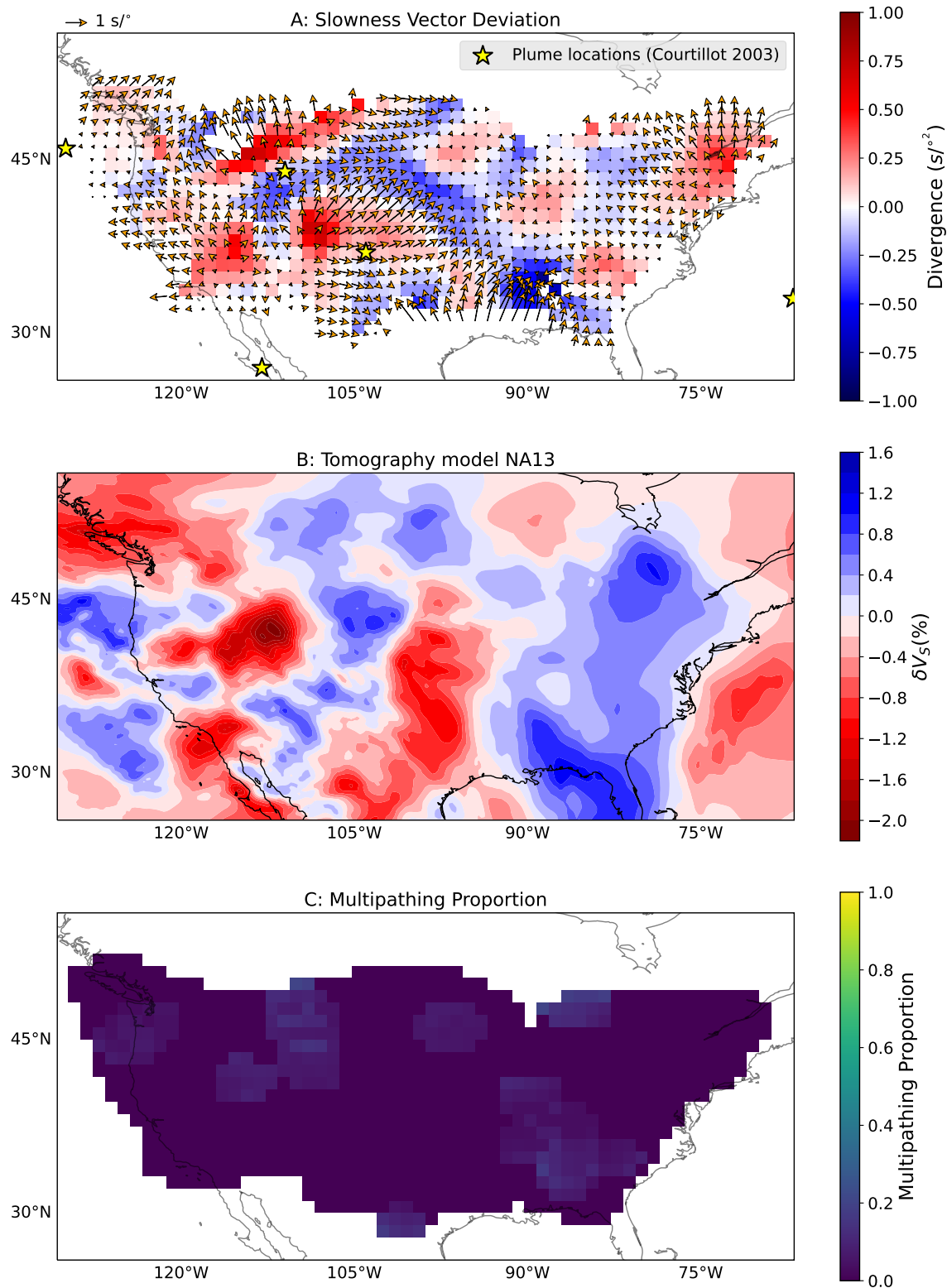


**Figure S12.** Summary plot for observations in the 0.10 – 0.20 Hz frequency band plotted at 1000 km depth.

May 25, 2023, 1:12pm

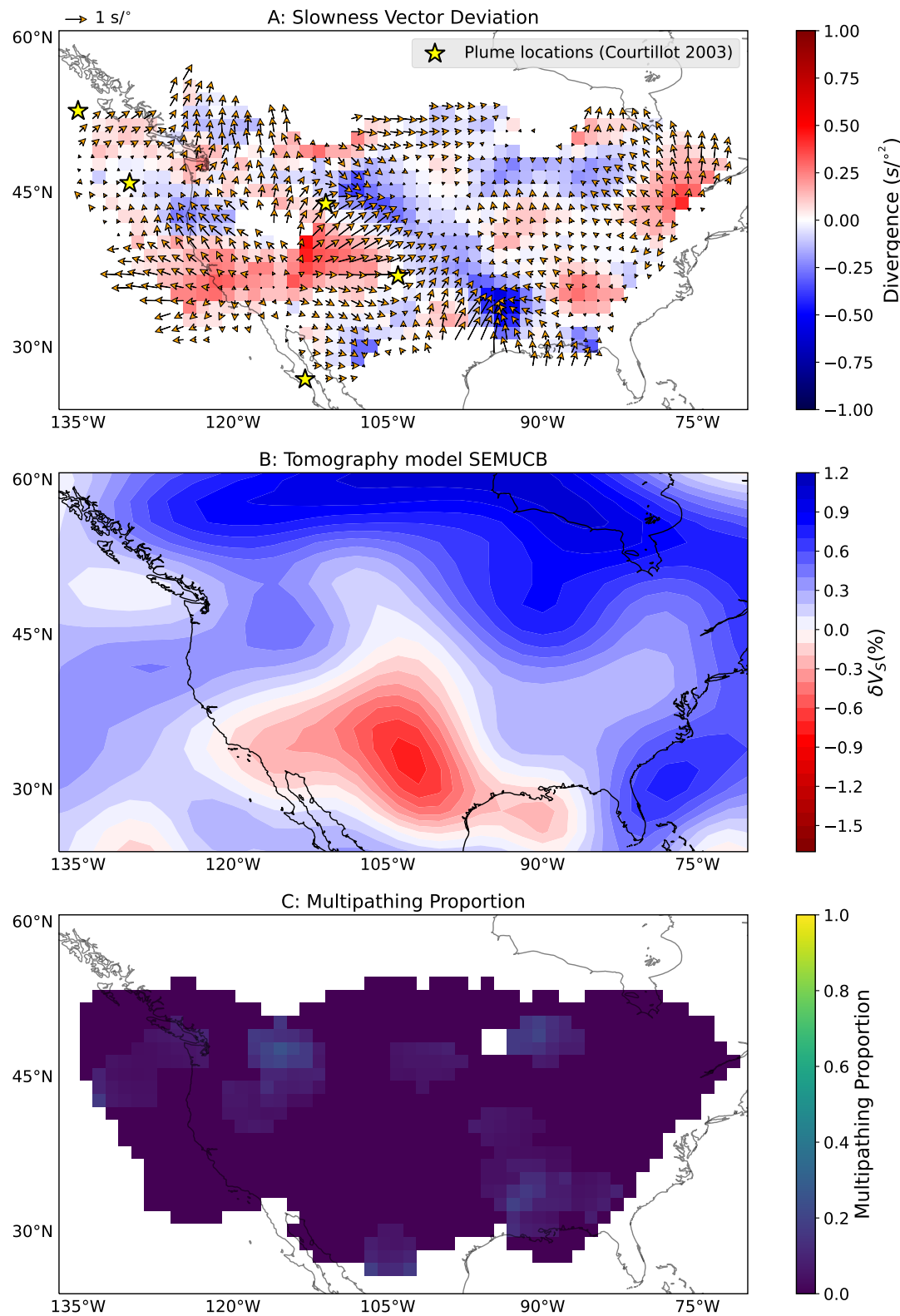


**Figure S13.** Summary plot for observations in the 0.10 – 0.20 Hz frequency band plotted at 1800 km depth.

May 25, 2023, 1:12pm

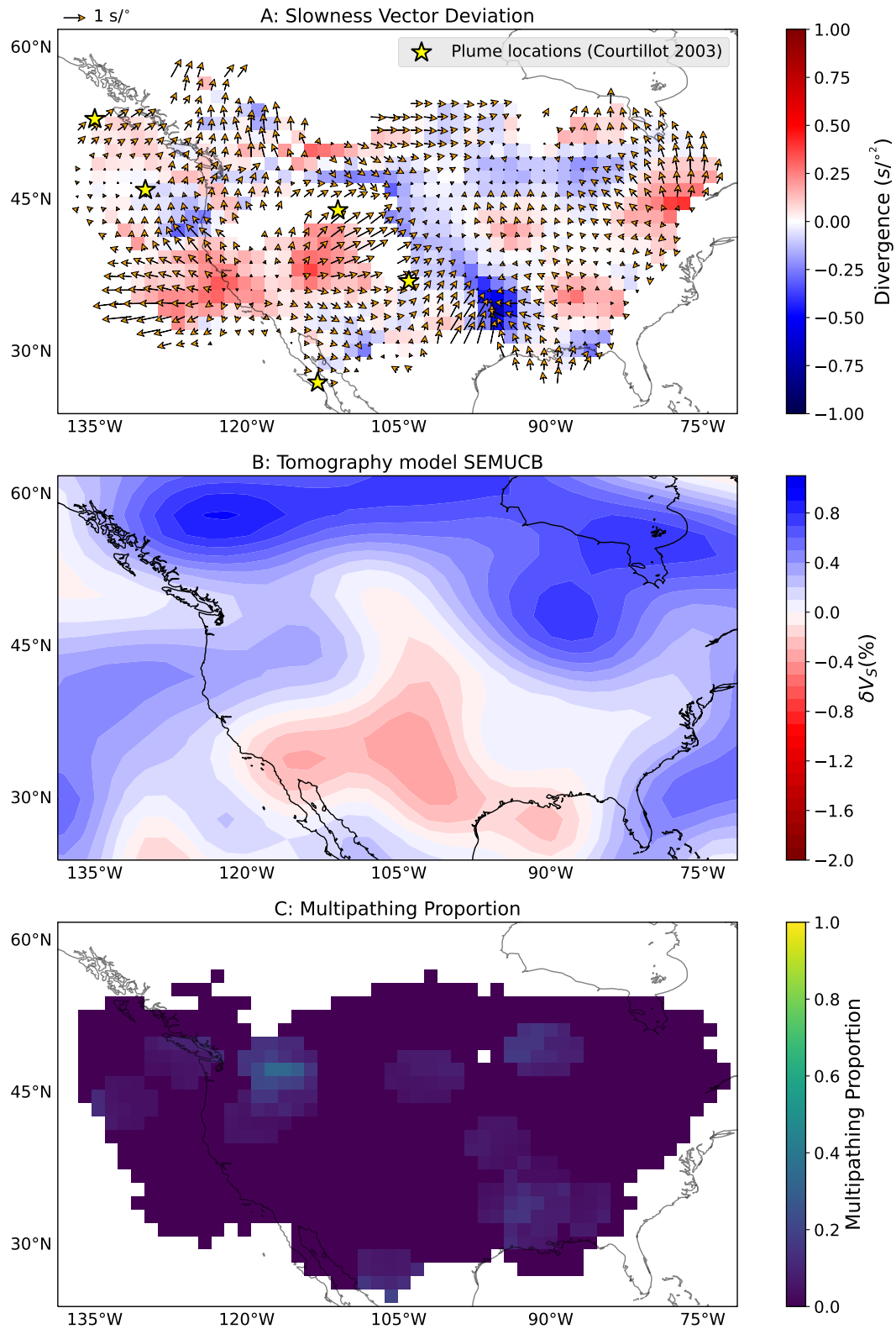


**Figure S14.** Summary plot for observations in the 0.10 – 0.20 Hz frequency band plotted at 2000 km depth.

May 25, 2023, 1:12pm

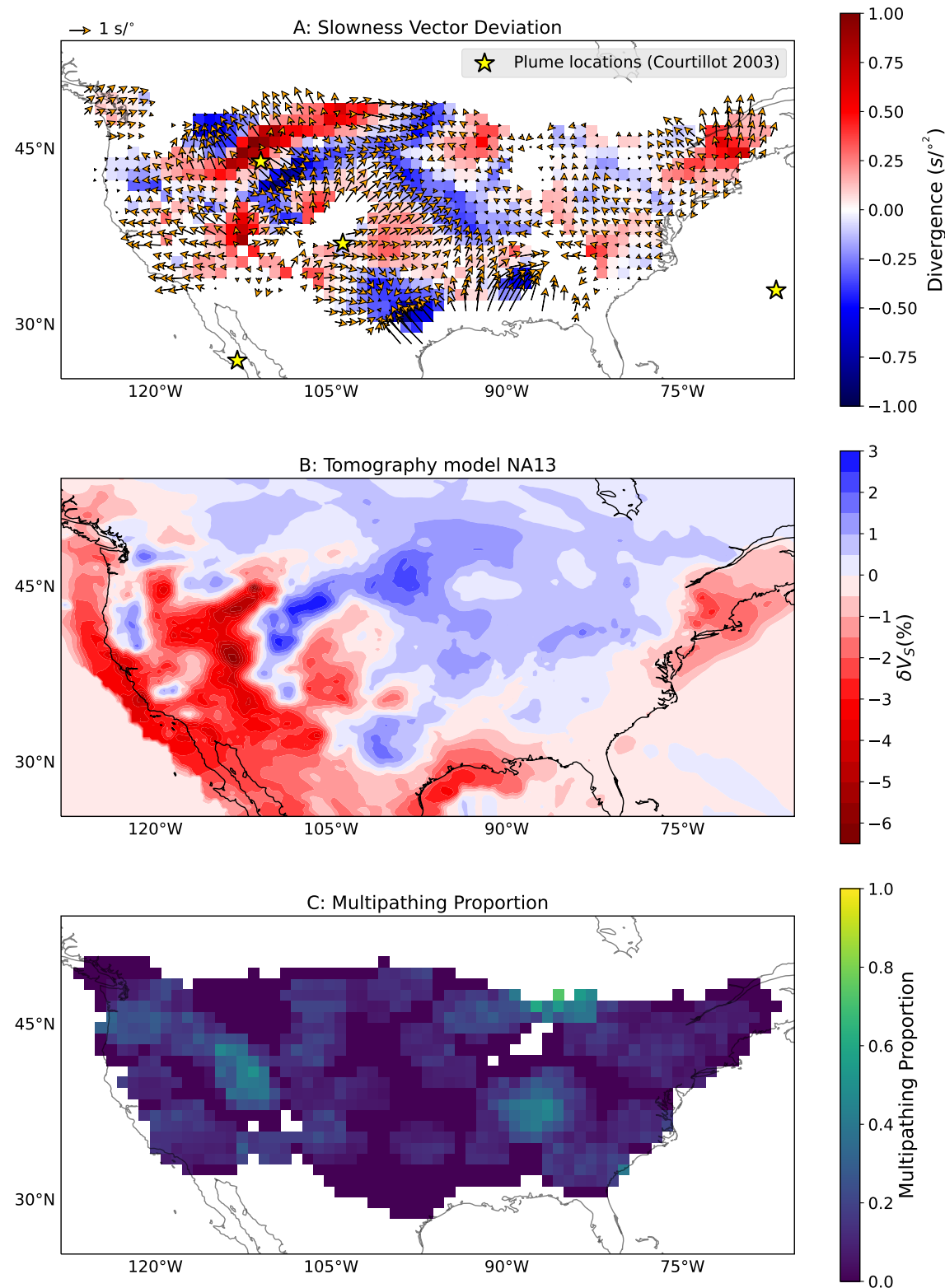


**Figure S15.** Summary plot for observations in the 0.15 – 0.30 Hz frequency band plotted at 200 km depth.

May 25, 2023, 1:12pm

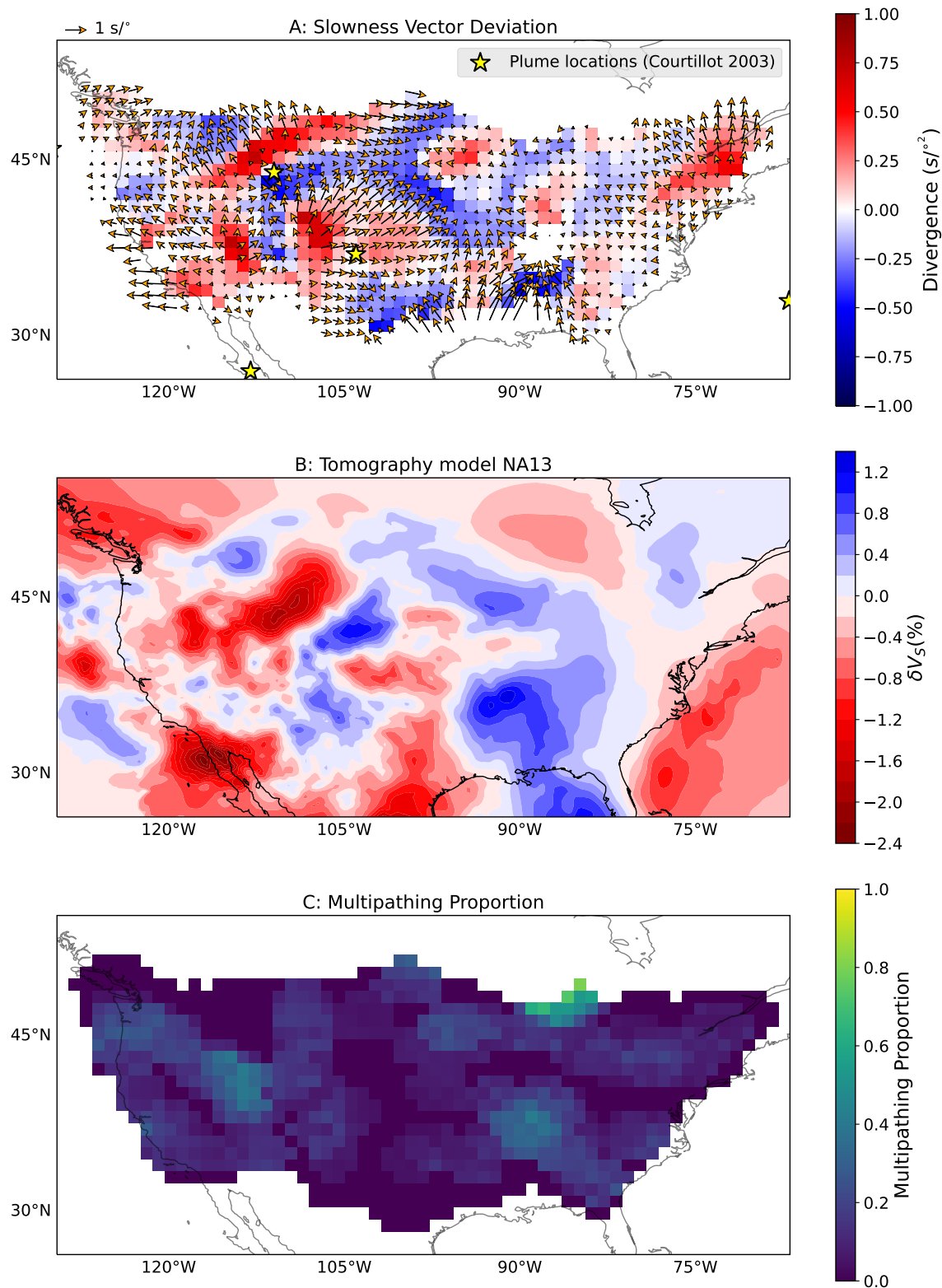


**Figure S16.** Summary plot for observations in the  $0.15 - 0.30 \text{ Hz}$  frequency band plotted at  $800 \text{ km}$  depth.

May 25, 2023, 1:12pm

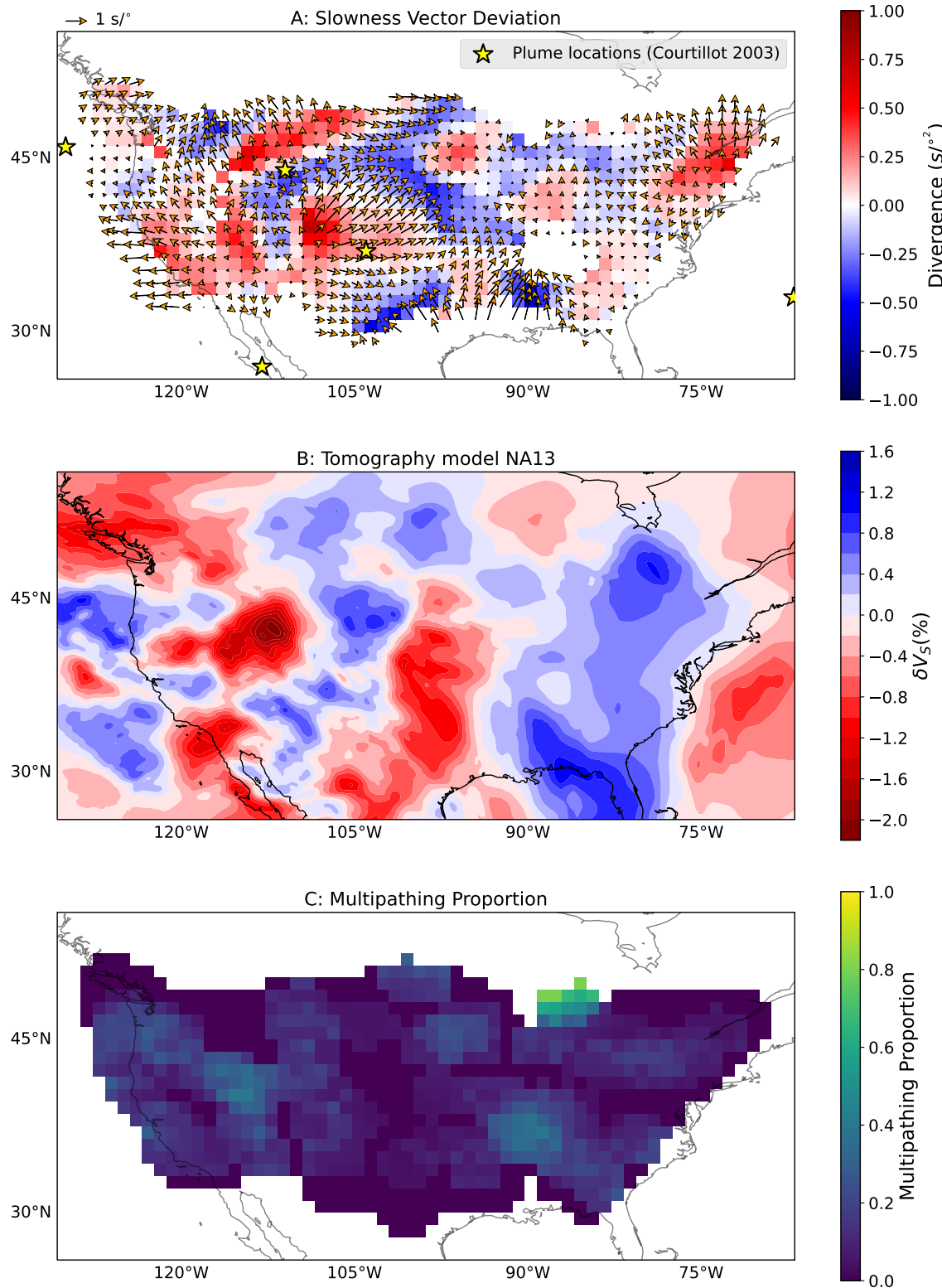


**Figure S17.** Summary plot for observations in the 0.15 – 0.30 Hz frequency band plotted at 1000 km depth.

May 25, 2023, 1:12pm

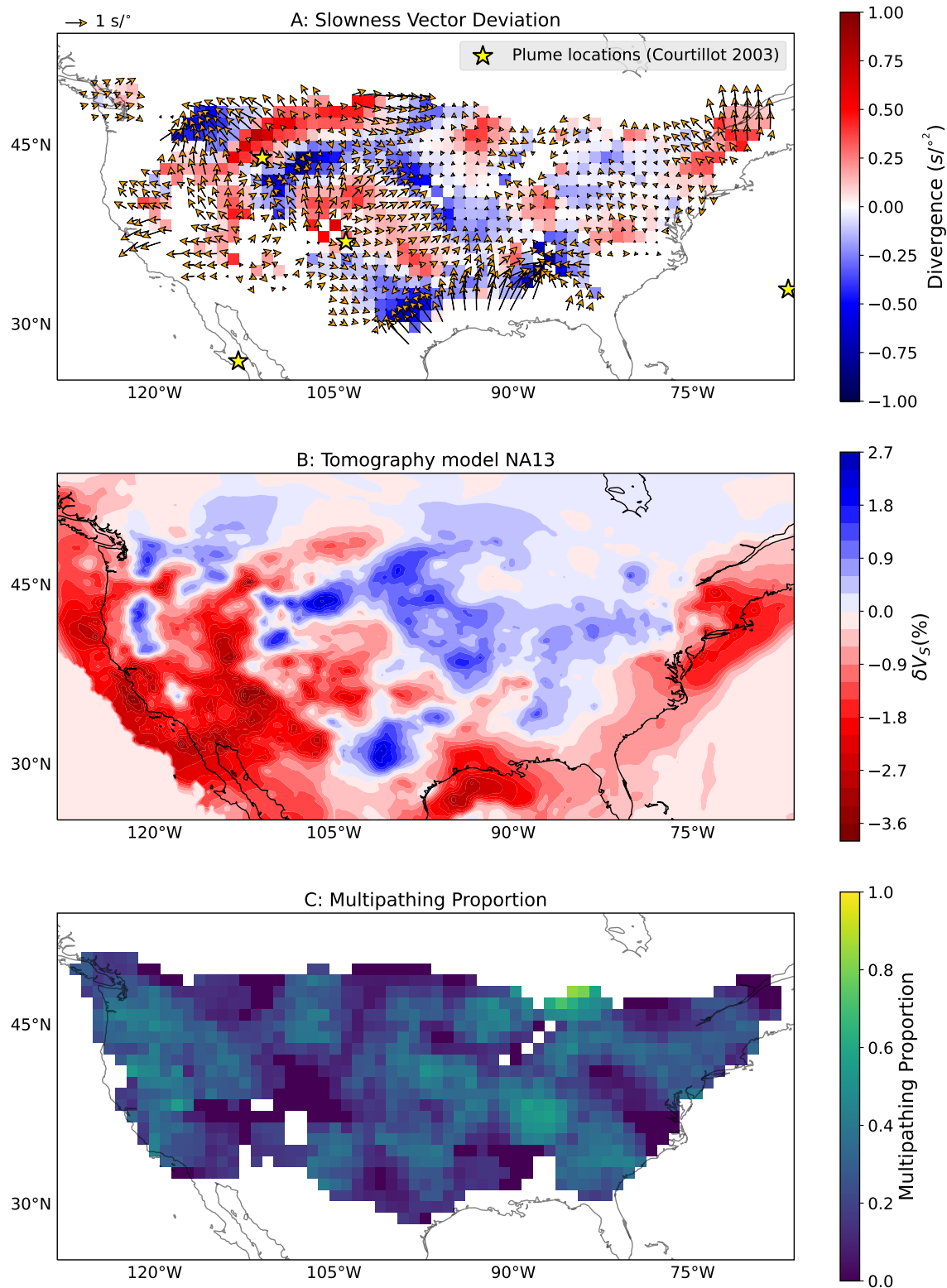


**Figure S18.** Summary plot for observations in the 0.2 – 0.40 Hz frequency band plotted at 300 km depth.

May 25, 2023, 1:12pm

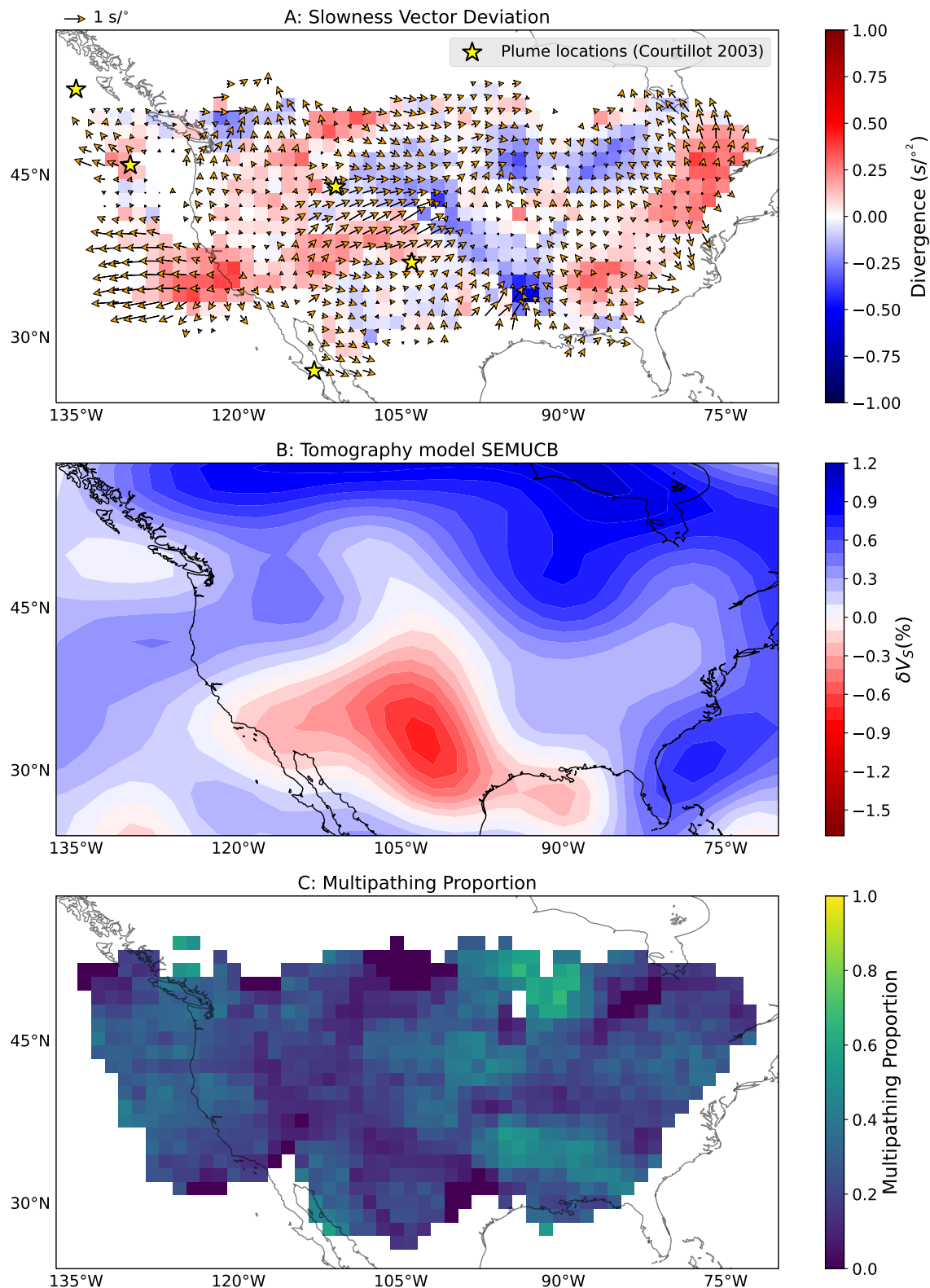


**Figure S19.** Summary plot for observations in the 0.2 – 0.40 Hz frequency band plotted at 1800 km depth.

May 25, 2023, 1:12pm